Drug Transport Modeling in Solid Tumors: a Computational Exploration of Spatial Heterogeneity of Biophysical Properties

Hooman Salavati (1,2,3), Pim Pullens (4,5,6), Wim Ceelen* (1,3), Charlotte Debbaut* (2,3)

(1) Department of Human Structure and Repair, Ghent University, Ghent, Belgium
(2) IBiTech–BioMMedA, Ghent University, Ghent, Belgium
(3) Cancer Research Institute Ghent (CRIG), Ghent, Belgium
(4) Department of Radiology, University Hospital Ghent, Ghent, Belgium
(5) Ghent Institute of Functional and Metabolic Imaging (GIFMI), Ghent University, Ghent, Belgium
(6) IBitech–Medisip, Ghent University, Ghent, Belgium
*Shared last authors

Corresponding author: HS (hooman.salavati@ugent.be)

Abstract

Inadequate uptake of therapeutic agents by tumor cells is still a major barrier in clinical cancer therapy. Mathematical modeling is a powerful tool to describe and investigate the transport phenomena involved. However, current models for interstitial flow and drug delivery in solid tumors have not yet embedded the existing heterogeneity of tumor biomechanical properties. The purpose of this study is to introduce a novel and more realistic methodology for computational models of solid tumor perfusion and drug delivery accounting for these regional heterogeneities as well as lymphatic drainage effects.

Several tumor geometries were studied using an advanced computational fluid dynamics (CFD) modeling approach of intratumor interstitial fluid flow and drug transport. Hereby, the following novelties were implemented: (i) the heterogeneity of tumor-specific hydraulic conductivity and capillary permeability; (ii) the effect of lymphatic drainage on interstitial fluid flow and drug penetration.

Tumor size and shape both have a crucial role on the interstitial fluid flow regime as well as drug transport illustrating a direct correlation with interstitial fluid pressure (IFP) and an inverse correlation with drug penetration, except for large tumors having a diameter larger than 50 mm. The results also suggest that the interstitial fluid flow and drug penetration in small tumors depend on tumor shape. A parameter study on the necrotic core size illustrated that the core effect (i.e. fluid flow and drug penetration alteration) was only profound in small tumors. Interestingly, the impact of a necrotic core on drug penetration differs depending on the tumor shape from having no effect in ideally spherical tumors to a clear effect in elliptical tumors with a necrotic core. A realistic presence of lymphatic vessels only slightly affected tumor perfusion, having no substantial effect on drug delivery.

In conclusion, our findings illustrated that our novel parametric CFD modeling strategy in combination with accurate profiling of heterogeneous tumor biophysical properties can provide a powerful tool for better insights into tumor perfusion and drug transport, enabling effective therapy planning.

Keywords: Interstitial fluid pressure; Drug transport; Biophysical properties of solid tumors; Computational fluid dynamics

1. Introduction

Cancer is a leading cause of death worldwide, accounting for about 10 million deaths in 2020 [1]. The most common cancers are solid tumors, which may demand a challenging course of treatment(s) [2, 3]. Unfortunately, the immediate surgical removal of solid tumors is often not an option for many tumor types due to pathological reasons (e.g. triggering metastasis) and/or the risk of severely damaging the host organ [4, 5]. Even in the case of complete or partial tumor resection, a favorable prognosis often depends on efficient follow-up treatments such as chemotherapy. In this context, despite the advancements of drug toxicity on cancer cells, resistance against drug delivery to the right location is a huge barrier for successful therapy [6]. Moreover, the systemic administration of chemotherapeutic agents may lead to unwanted side effects damaging normal cells and causing drug resistance [7]. Hence, all of the above points result in a growing interest for targeted and locoregional chemotherapy, aiming at treating the tumor while sparing healthy tissues.

Limitations of drug delivery to intended tissues have been correlated to hostile biophysical characteristics in the solid tumor microenvironment. On one hand, the newly-formed blood vessel network in solid tumors is typically characterized by high heterogeneity, structural abnormalities, and extreme leakiness [8, 9]. The latter causes a high influx of interstitial fluid into the tumor interstitium,

which - in the absence of a fully functional and normal lymphatic network to drain excess fluid - results in a great imbalance of tumor perfusion [10]. This phenomenon is typically characterized by a noticeably high interstitial fluid pressure in tumors (IFP; in the range of 10-100 mmHg) compared to normal tissues (range of 0-5 mmHg) [3, 11]. On the other hand, it has been observed that the vascular network density may decrease as a tumor grows, generating a hypoxic region [9]. Persisting hypoxia in the tumor center frequently results in the formation of a necrotic core, which is believed to be harder to treat as it underlies several malignant processes such as angiogenesis and metastasis [12].

Despite the knowledge on the importance of solid tumor biophysics on the outcome of cancer therapy, the details of tumor dynamics are still largely unknown, mainly due to remaining challenges to quantify these effects and the corresponding relevant parameters [13]. For instance, the difficulties of intratumor IFP profiling using direct (experimental) methods hindered comprehensive studies of drug delivery to tumors [3]. In this context, mathematical modeling and computational simulations have been recommended as powerful cost-effective tools to reveal various aspects of treatments (e.g. drug transport) in solid tumors [14].

Baxter and Jain [15, 16] were the first to develop a theoretical model of tumor perfusion based on Darcy's law, which showed that IFP in a homogeneous tumor without lymphatics was elevated, reaching a plateau value in the center of the tumor, with a steep downward gradient near the periphery. They suggested that the presence of a necrotic core had a negligible effect on IFP unless it exceeded more than 90% of the tumor radius. Additionally, the fully functional lymphatic network within the tumor would only lower the maximum interstitial fluid pressure. With a similar framework, Sarntinoranont et al. [17] considered the gradual transition in material properties at the tumor-normal tissue interface by implementing prescribed spatially dependent profiles, which resulted in a less steep IFP transition at the tumor border compared to the results obtained by Baxter and Jain [16]. Multiple other works [18-23] estimated the spatial variation of tumor vascular properties and reconstructed a realistic image-based tumor geometry. These studies generally resulted in smaller and more heterogenous IFP values compared to Baxter and Jain's results due to inclusion of low vascular filtration zones in the tumor (e.g. necrotic core).

Milosevic et al. [24] reported that although the IFP in solid tumors follows the microvascular pressure, the variation of IFP in different tumors is caused by a combination of parameters including the differences in capillary resistance to blood flow, interstitial hydraulic conductivity, and tumor elasticity [25]. Tang et al. [26] presented a 3D representation of tumor growth coupled with angiogenesis based on empirical methods, in which the authors established a relative relation between IFP and tumor shape. Sefidgar et al. [27] also evaluated the importance of tumor shape on IFP, and illustrated that the maximum IFP does not necessarily happens in the center of the tumor depending on the shape of tumor. The author also predicted that the IFP is insensitive to the tumor size in small tumors (below 1 cm^3). Furthermore, d'Esposito et al. [28] also showed that IFP is heterogenous in the center of the tumor, with IFP variations up to 10 mmHg. The authors later concluded that lowering the IFP is not the key factor for normalizing interstitial perfusion, which is necessary in efficient chemotherapy [29]. The results previously obtained in our group by Steuperaert et al. [23, 30] for intraperitoneal chemotherapy confirmed the correlation between tumor size and IFP, and further suggested that the presence of a necrotic core in small tumors reduces the IFP, whereas it does not alter the IFP in larger tumors. Another conclusion was that the tumor size does not seem to correlate with the IFP in heterogeneously perfused tumors [23]. Similarly, LoCastro et al. [31, 32] defined a significant relation between IFP and tumor size in patients with head and neck tumors.

To this date, as indicated above, only a few studies have partly elaborated on the effect of tumor perfusion (i.e. interstitial fluid source, flow and drainage) and the presence of a necrotic core [33].

Furthermore, the heterogeneity of the tumor's hydraulic conductivity and vascular permeability was not accounted for. In contrast to the assumptions in literature [15, 16, 21, 22, 27, 30, 34, 35], the hydraulic conductivity and corresponding permeability of solid tumors do not have a uniform value inside tumors [36]. This was confirmed by experimental studies illustrating a noticeable heterogeneity in hydraulic conductivity values [37, 38]. Similarly, the vessel hydraulic conductivity or leakiness is (even more) heterogenous [29], requiring a realistic profiling. On the other hand, despite the observation of the partial presence of lymph vessels in the periphery of solid tumors, the impact of intratumor lymphatics has not received any thorough investigation yet. Therefore, in the current study, a CFD model of interstitial fluid flow and drug transport was developed to account for spatial heterogeneity of tumor biophysical properties, focusing on the hydraulic conductivity and the vascular permeability. Using this CFD approach, the impact of tumor geometry, necrotic cores, and lymphatic vessels was investigated using a parameter study considering (i) a parametric tumor geometry to study different tumor sizes, shapes and configurations, (ii) different necrotic core sizes and locations, and (iii) the transition from alymphatic regions to tissue with normal lymphatics.

2. Method

Several tumor geometries were created incorporating necrotic, hypoxic, and viable regions. The spatial heterogeneity of three key transport properties - vascular permeability, hydraulic conductivity, and lymphatic drainage rate - were defined and implemented into the physical models (i.e. Darcy's and Starling's laws coupled with the advection-diffusion equation) to simulate interstitial fluid flow and drug delivery in solid tumors.

2a. Tumor geometry and boundary conditions

A tumor embedded in surrounding normal tissue is considered for all cases in the current study. Solid tumors as well as their corresponding necrotic cores have a large variety in shape and size [30, 39], but they are mostly considered to be roughly round-shaped [27]. Therefore, three different types of 3D tumor geometries with a parametric diameter $Ø_p$ [m] (Fig. 1; with $Ø_p=2R_p$) were created comprising an outer viable zone, a hypoxic zone, and a necrotic core. The first type of geometries (Fig. 1a) consists of symmetric spherical tumors (SST) with a necrotic core of diameter $Ø_n$, where neither viable cells nor functional vascular or lymphatic vessels are present. The intermediate hypoxic region is characterized by functional blood capillaries, but no functional lymphatic vessels. Finally, in the viable zone, living cells, functional capillaries and functional lymphatic vessels are present.

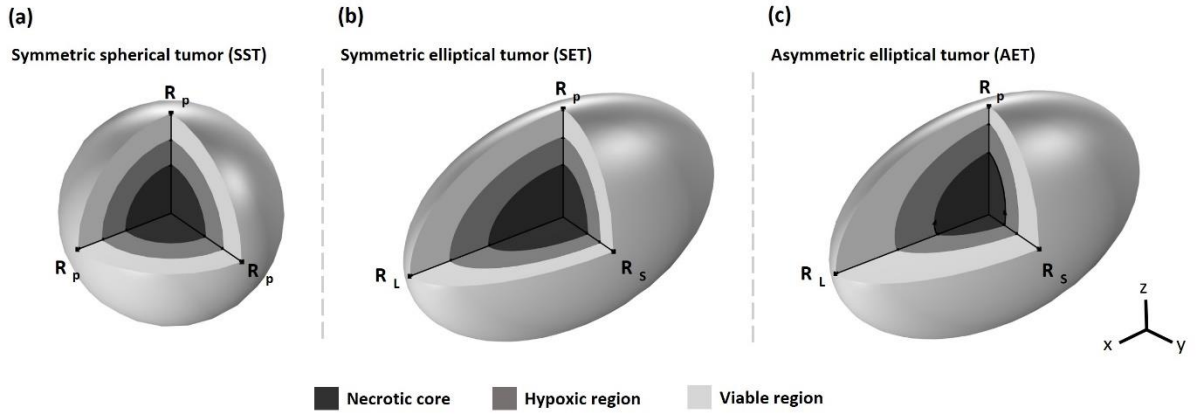

Fig 1. Three types of tumor model geometries comprising the necrotic core (black region), hypoxic region (dark gray region) and viable region (light gray region) in 3D. **(a)** Symmetric spherical tumor (SST). **(b)** Symmetric elliptical tumor (SET). **(c)** Asymmetric elliptical tumor (AET).

Similarly, a symmetric ellipsoidal tumor geometry (SET; Fig. 1b) was created with the same volume as the spherical tumor ($\emptyset_p = \frac{2}{3}\emptyset_L = \frac{3}{2}\emptyset_s$ with $\emptyset_L$ [m] and $\emptyset_S$ [m] being the long and short axis length, respectively) to investigate the effect of shape on tumor perfusion and drug delivery. Finally, also an asymmetric elliptical tumor (AET; Fig. 1c) was created by shifting the necrotic core and hypoxic region (over a distance of $R_n/3$, $R_n/5$ and $R_n/4$ in the X, Y and Z direction, respectively), as a more realistic tumor geometry. In order to investigate the role of the necrotic core on interstitial fluid flow, four different necrotic core volumes were modeled according to the necrotic core ratio ($n_r=R_n/R_p$) comprising a viable (non-necrotic; $n_r=0$) tumor and three necrotic tumors with n_r values of 0.25 (small core), 0.5 (medium core) and 0.75 (large core). In all geometries (SST, SET, AET), the outer radius of the intermediate hypoxic region is the average of the viable and necrotic region radii ($\emptyset_h = 2R_h = \frac{\emptyset_p+\emptyset_n}{2}$). To investigate tumor size implications, six cases were defined ($\emptyset_p$ ranging between 1 to 50 mm) on a baseline geometry having a n_r of 0.50 and no lymphatic vessels. For studying the necrotic core and lymphatic drainage effects, two baseline alymphatic tumors were generated with diameters of 5 mm (small tumor) and 50 mm (large tumor).

2b. Tumor perfusion model

The transport of interstitial fluid into normal tissue interstitium is organized as a balance between an inward flow of interstitial fluid from the vascular capillaries towards the interstitium, and an outward absorption from the interstitium into the lymphatic capillaries [16]. In solid tumors, this balance is lost mainly due to the abnormally high permeability of the leaky tumor capillary network. Considering tumor tissue as an isotropic porous medium, the corresponding interstitial fluid flow and IFP interplay can be described by Darcy's law (Eq. 1), for which the hydraulic conductivity *K(r)* [m^2/Pa·s] depends on the local tissue permeability *k(r)* [m^2] *and* μ [Pa·s] the interstitial fluid dynamic viscosity [16] (Eq. 2). Hereby, u_i[m/s] represents the interstitial fluid velocity (IFV) vector, p_i [Pa] the interstitial fluid pressure (IFP), and *r* [m] the radial coordinate.

$$u_i = -K(r)\,\nabla \mathrm{p}_i \qquad \text{(Eq. 1)}$$

$$K(r) = \frac{k(r)}{\mu} \qquad \text{(Eq. 2)}$$

Regarding the heterogeneity of *K* in solid tumors as shown in [37, 40-43], assigning a piecewise K profile (Fig. 2a) would be a more accurate representation of the real case compared to current constant values used over the complete tumor geometry [37, 44]. Moreover, almost all previous works focusing on simulating the interstitial fluid flow in solid tumors [14-16, 21, 23, 26, 30-32, 45, 46] assumed that the hydraulic conductivity of tumor tissue is generally higher than normal tissue. However, it has been reported that the hydraulic conductivity of tumor interstitium can be either lower or higher than normal tissue depending on the tumor type [37, 44, 47]. Furthermore, several inverse correlations have been found between the hydraulic conductivity and the tissue microenvironment elements such as the concentration of collagen fiber and glycosaminoglycan [48-50]. Regarding the higher concentration of these elements in solid tumors [51, 52], the assumption of lower values of hydraulic conductivity inside solid tumors compared to normal tissue is more plausible (as shown in our previous work [37]).

Following a similar approach as done in [44], a radius-dependent profile was considered for hydraulic conductivity in the models (Fig. 2a; for a tumor with $n_r=0.5$), where *K* has a constant value inside the

necrotic core. Moving from the necrotic core surface (r/R=0.5 for the baseline model) to the edge of the vital region (r/R=0.75 for the baseline model), *K* decreases to a fixed value, and then it increases again to a maximum value at the border of the tumor and the normal tissue (r/R=1). It should be considered that depending on the necrotic core size, the locations of the turning points (i.e. at the borders of necrotic core and hypoxic regions) is different in each case.

Next to Darcy's law, the continuity equation represents the conservation of mass for the interstitial flow:

$$\nabla \cdot \mathrm{u}_i = J \qquad \text{(Eq. 3)}$$

for which J [1/s] is the rate of interstitial fluid generation or drainage. The fluid source term is a combination of fluid inflow originating from vascular capillaries (J_v $[1/\mathrm{s}]$) and outflow through lymphatic capillaries by means of lymphatic drainage from the interstitial space (J_l $[1/\mathrm{s}]$).

$$J = J_v - J_l \qquad \text{(Eq. 4)}$$

J_v can be described by Starling's law as follows [53]:

$$J_v = L_p(r)\frac{S}{V}(p_v - p_i - \sigma(\pi_v - \pi_i)) \qquad \text{(Eq. 5)}$$

for which $L_p(r)$ [m/Pa·s] represents the local hydraulic conductivity of the vasculature, S/V [1/m] is the surface area of blood capillaries per unit volume. Furthermore, p_v [Pa], p_i [Pa], σ [-] , π_v [Pa] and π_i [Pa] represent the vascular pressure, interstitial fluid pressure, osmotic reflection coefficient, vascular and interstitial osmotic pressure, respectively. The blood vessel's hydraulic conductivity or leakiness is also highly heterogenous across the tumor microvasculature [29], requiring a realistic profiling. Several studies reported a radially outward increase of microvascular density in solid tumors [54-56], resulting in a higher extravasation of interstitial fluid close to the surface of tumor. According to suggestions of [57] based on reported values of vascular permeability in the literature, an exponential function, $L_p(r) = \frac{r-R_n}{R_p-R_n}e^{\frac{r}{R_p}-1}$, was selected to mimic the radius-dependent profiles for permeability and density of the tumoral capillary network (Fig. 2b; n_r=0.5). Accordingly, having no blood capillary in the necrotic core ($L_p(r) = 0$), $L_p(r)$ increases to a maximum value of $L_{p_{max}}$ at the tumor edge, and decreases again to the permeability value in normal tissue.

There have been two main approaches to determine J_l in the literature. The majority of studies considered that due to absence of functional lymphatic vessels in the tumor interstitium, the lymphatic drainage is negligible (i.e. J_l=0 [1/s]) [14, 16, 21-23, 27, 58]. A limited number of studies also described the presence of lymphatics inside tumors, in which no lymph vessels are present in the central region (i.e. necrotic core), but an active lymphatic drainage network does exist in the remaining areas of the tumor [15, 59]. However, the hard transition from alymphatic to lymphatic regions does not reflect a realistic implementation, from which it is known that these properties change gradually [17, 44]. Although it is believed that no fully-functional lymphatics are present in solid tumors, several works have reported the partial presence of lymph network at the periphery of solid tumors [60-62]. If so, even an impaired lymphatic network would affect the solid tumor perfusion. Mathematically, this can be described as follows [15]:

$$J_l = f_L(p_i - p_L) \qquad \text{(Eq. 6)}$$

$$f_L = L_{p_L}(r)\frac{S_L}{V_L} \quad \text{(Eq. 7)}$$

for which $L_{p_L}(r)$ [m/Pa.s] represents the local hydraulic conductivity of lymphatic vessel walls, S_L/V_L [1/m] is the surface area of lymphatic vessels per unit volume, p_L [Pa] is the effective lymphatic pressure. Accordingly, along with the alymphatic tumor, three exponential profiles, $L_{p_L}(r) = \frac{r-R_i}{R_p-R_i}e^{a(\frac{r}{R_p}-1)}$ with a=(2,10,50), were designed to describe the presence of lymph vessels inside solid tumors (Fig. 2c; n_r=0.5). In all cases, no functional lymphatic vessels exist in the necrotic core and hypoxic region. In the viable region, it was assumed that the activity of the lymphatic network exponentially increases while moving towards the tumor edge.

2c. Drug transport model

Drug delivery to solid tumors happens by two mechanisms, namely diffusion and convection. The diffusive part is due to the concentration gradient, whereas the convective part is governed by the interstitial fluid flow and corresponding pressure gradients. Taking into account drug extravasation from blood vessels (φ_v), drug drainage from the interstitial space via lymph vessels (φ_l) as well as drug cellular binding (φ_b), the drug transport model can be described as [16]:

$$\frac{dc}{dt} = D\nabla^2 c - \nabla\cdot(u_i c) + \varphi_v - \varphi_l \quad \text{(Eq. 8)}$$

Where c [mol/m^3] and D [m^2/s] are the interstitial drug concentration and the drug effective diffusion coefficient, respectively. The φ_v and φ_l are given by the following equations as found in [16]:

$$\varphi_v = v\frac{S}{V}(c_p - c)\left(\frac{Pe}{e^{Pe}-1}\right) + J_v(1-\sigma_d)c \quad \text{(Eq. 9)}$$

$$\varphi_l = J_l c \quad \text{(Eq. 10)}$$

for which v [m/s] is the vascular permeability to drug coefficient, c_p [mol/m^3] is the plasma concentration of the drug and σ_d [-] is the solvent-drag reflection coefficient describing the ease of drug molecules transport through the vasculature [30]. Pe [-], the Peclet number, is representing the ratio of convective transport to diffusive drug transport, and it is expressed by:

$$Pe = \frac{J_v(1-\sigma_d)}{v\,S/V} \quad \text{(Eq. 11)}$$

Since the therapeutic time window is quite small during bolus administration (usually 30 minutes to an hour) and the tumor volume is considerably smaller than the total body volume [30], it is assumed that the plasma concentration of the drug (c_p) would remain insignificant throughout the simulations.

The values of the parameters used in the models are summarized in Table 1. The interstitial fluid flow and drug transport throughout tumors were simulated in COMSOL Multiphysics (Inc., Burlington) using all described geometries. A finite element method (FEM) solver was used to numerically solve the equations of the fluid flow and the drug transport by means of discretization via quadratic and linear methods, respectively. The MUMPS (Multifrontal Massively Parallel Sparse Direct Solver) system solver was used to solve the interstitial flow and drug concentration terms and obtain the solution in a segregated direct manner. The relative tolerance was set to 0.01 to ensure computational efficiency. To ensure grid independence, the mesh parameters were tested on the largest AET (AET Ø50) using

four different grids. Based on the resulting IFP and concentration profiles, the optimal grid, with coarser elements in the normal tissue, consisted of 72,702 tetrahedral volume elements and 65,440 prism elements in the boundary layers along the tumor and normal tissue boundary. Similar mesh settings were applied to the remaining tumor geometries.

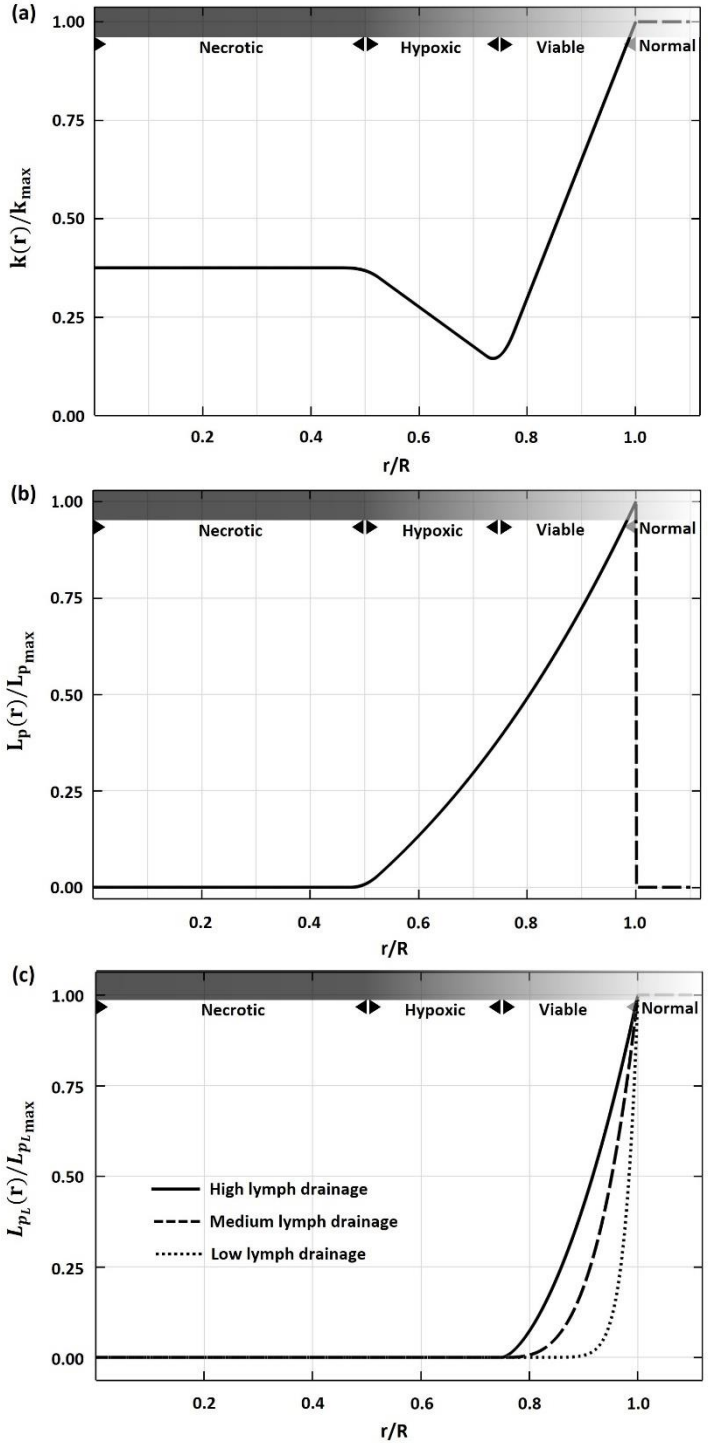

Fig 2. Map of spatial heterogeneity of tumor biophysical properties in the model throughout tumor and normal tissue **(a)** Spatial variation of tumor tissue permeability, $k(r)$. **(b)** variation of tumor vascular permeability, $L_p(r)$. **(c)** Map of lymphatic vessels presence inside the solid tumor and normal tissue, $L_{p_L}(r)$. Three cases were defined for high, medium and low lymphatic drainage in solid tumors.

Table 1. Parameter values used for baseline simulation

Parameter	Description		Baseline value	Value range	Reference
$k_{max}\ [m^2]$	Normal tissue permeability	Tumor Normal	2.8×10^{-16}	$(0.4 - 2.8) \times 10^{-16}$	[37]
$\mu\ [Pa\ s]$	Interstitial fluid viscosity	Tumor Normal	3.5×10^{-3}	-	[63]
$L_{p_{max}}\ [m/Pa\ s]$	Vessel maximum permeability	Tumor Normal	2.1×10^{-11} 2.7×10^{-12}	$(0.0 - 2.1) \times 10^{-11}$ -	[16]
$S/V\ [m^{-1}]$	Vessel surface area per unit volume	Tumor Normal	7.0×10^{3} 2.0×10^{4}	- -	[16]
$p_v\ [Pa]$	Microvascular pressure	Tumor Normal	2080	-	[16]
$\pi_v\ [Pa]$	Vascular osmotic pressure	Tumor Normal	2666	-	[16]
$\pi_i\ [Pa]$	Interstitial osmotic pressure	Tumor Normal	2000 1333	- -	[16]
σ	Osmotic reflection coefficient	Tumor Normal	0.8 0.9	- -	[16]
$f_{l_{max}}\ [1/Pa\ s]$	Lymphatic filtration coefficient	Tumor Normal	1.0×10^{-7}	$(0.0 - 1.0) \times 10^{-7}$	[18]
$p_L\ [Pa]$	Lymphatic pressure	Tumor Normal	0.0	- -	[16]
$D\ [m^2/s]$	Diffusion coefficient	Tumor Normal	2.5×10^{-10}	-	[30]
$v\ [m/s]$	Permeability of vessel to drug	Tumor Normal	1.7×10^{-8} 2.2×10^{-9}	- -	[16]
σ_D	Reflection coefficient of vessels for drug	Tumor Normal	0.9	-	[16]

2d. Boundary conditions

The computational domain comprises the solid tumor embedded in the center of a cuboid normal tissue, with sides four times larger than the corresponding diameter of the tumor (i.e. $Ø_p$, $Ø_L$ and $Ø_s$). The pressure was assigned to be equal to normal IFP (i.e. 0 mmHg) at the border of the computational domain, far from the tumor edge to cancel the border effect. A fixed drug concentration (i.e. 0.17 mol/m^3 of the cytotoxic agent cisplatin used for intraperitoneal chemotherapy) was assumed to exist at the edge of the tumor to evaluate the penetration depth. The continuity of interstitial pressure, interstitial velocity (pressure gradient) as well as the concentration and its flux were assigned at the boundary between the tumor and the surrounding normal tissue.

2e. Parameter study

The baseline values in Table 1 combined with the profiles illustrated in Fig. 2 are used for all simulations (Table 2). In order to investigate the sensitivity of the modeling strategy to certain modelling parameters, a parameter study was conducted for variations in tumor size, necrotic core size, tumor shape, tumor configuration (i.e. asymmetric location of necrotic core and hypoxic region inside tumor) and lymphatic drainage presence.

The effect of tumor size on tumor perfusion was independently investigated in a baseline case (alymphatic tumor; n_r=0.5) in each geometrical category with total diameters ranging between 1-50 mm. Accordingly, six different volumes were defined in each shape category (i.e. SST, SET and AET), with the generic diameter ($Ø_p$) ranging from 1 to 50 mm (Table 2).

Table 2. An overview of all investigated cases

Tumor shape	Tumor diameter [mm]	Necrotic core diameter [mm] (n_r)	Lymph presence
SST SET AET	1.0	0.5 (0.50)	-
	3.0	1.5 (0.50)	-
	5.0	0.0 (0.00)	-
		1.25 (0.25)	-
		2.5 (0.50)	High, medium, low and no lymph drainage
		3.75 (0.75)	-
	10.0	5.0 (0.50)	-
	20.0	10.0 (0.50)	-
	50.0	0.0 (0.00)	-
		12.5 (0.50)	-
		25.0 (0.50)	High, medium, low and no lymph drainage
		37.5 (0.75)	-

The presence of the necrotic core and its effect on the IFP, IFV and drug concentration was also explored. Accordingly, four cases were defined including a non-necrotic tumor (i.e. n_r= 0.00) and three necrotic tumors. Also, four cases were considered, including an alymphatic tumor and three lymphatic cases with different filtration rates (Fig. 2c).

3. Results

The results of the simulation were analyzed using 3D and 2D contours (Fig. 3a-c) and 1D plots (Fig. 3d-e) for one case (AETØ10). The maximums of IFP (IFP_{max}) and IFV (IFV_{max}) were defined according to the highest values among all cases (Table 2). In addition to comparing the highest value of IFP observed in each case, another variable was also defined to illustrate where IFP maintained values over 50% of the tumor-specific highest IFP (IFP50%; Fig. 3d). The penetration depth was investigated by defining the penetration depth index (PDI) as the percentage of the radius (r) where drug concentration values exceed the corresponding half-maximal (50%) inhibitory concentration (IC50; Fig. 3e) equal to 6.2 mol/m^3 [30].

Along with the introduced heterogeneous model (Fig 3; solid black lines in panels d-e), the homogenous counterpart of the AETØ10 was also illustrated (Fig. 3d-e; dashed orange lines), in which the value of Lp is constant ($L_{p_{max}}$) in the tumor. Also, the value of K in the tumor was equal to K in the necrotic core and K in normal tissue equal to K_{max} (Fig. 2a). A noticeable difference was observed between the IFP profiles of heterogenous and homogenous tumors, not specifically in the highest IFP but in the trend as well as IFP50% locations. The drug penetration depth is slightly higher when assuming homogenous properties, increasing the PDI.

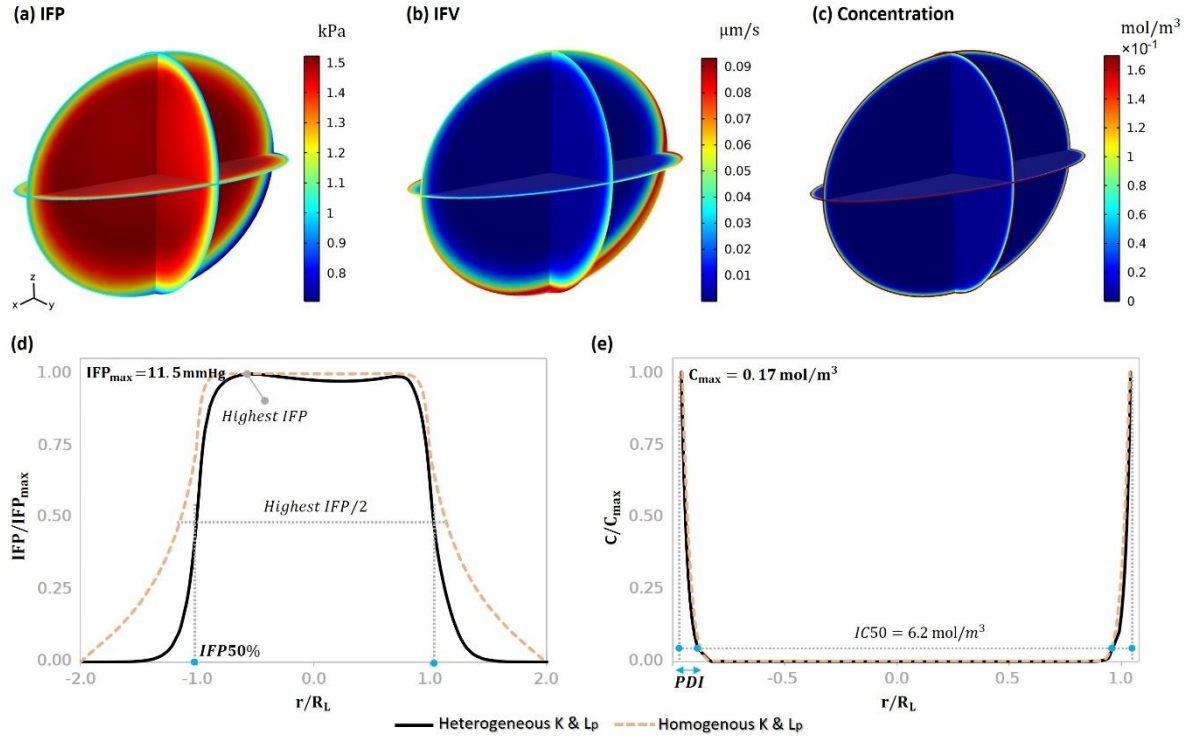

Fig 3. (a-c) 3D contour plots of IFP, IFV and drug concentration in AETØ10 (alymphatic, n_r=0.50) with heterogenous properties, and **(d-e)** analyzed parameters on 1D plots of IFP and concentration on the long axis of the AETØ10 with heterogenous (solid lines) and homogenous (dashed lines) properties.

3a. Tumor size and shape

Fig. 4a illustrates the tumor size correlation with the IFP in the SST category, demonstrating a central plateau profile of IFP in all cases. The maximum IFP (11.5 mmHg) value does not noticeably change in tumors with a diameter larger than 20 mm, whereas the maximum IFP is clearly lower for tumors with a diameter smaller than 10 mm (e.g. a small nodule with 1 mm diameter can only get to 1.3 mmHg). The minimum IFP seen in each SST case maintained a value of more than 50% of the highest IFP (IFP50%) estimated in each case, where the IFP50% located between 0.1 mm (in SSTØ1) to 3 mm (in SSTØ50) from the surface of the tumor. Furthermore, the IFP remains higher than normal tissue even beyond the tumor surface. Interestingly, the elevated IFV is more persistent in smaller tumors (Fig. 4b). Regarding the highest value of IFV in each SST case, for all tumors the highest value was on the border of the tumor and the normal tissue, however, only the largest tumor (SSTØ50) gained the maximum value (0.1 μm/s) while others reached 95%, 89%, 81%, 74% and 44% of the maximum IFV, respectively SSTØ20 to SSTØ1. In all cases, the interstitial fluid flow only existed outside of the necrotic core, however, results showed as the tumor gets larger the normalized extent of non-zero IFV decreases.

In all cases, the drug penetration depth (Fig. 4c) depends on tumor size, with deeper penetration in smaller tumors. Interestingly, only in the smallest tumor (SSTØ1), the drug penetrates all over the tumor, in which the minimum concentration of the field was about 20% of the maximum concentration. The PDI ranged between 1% for the largest tumor (SSTØ50) to 23% for SSTØ3. For SSTØ5, SSTØ10 and SSTØ20, the PDI's were 13%, 7%, 3%, respectively.

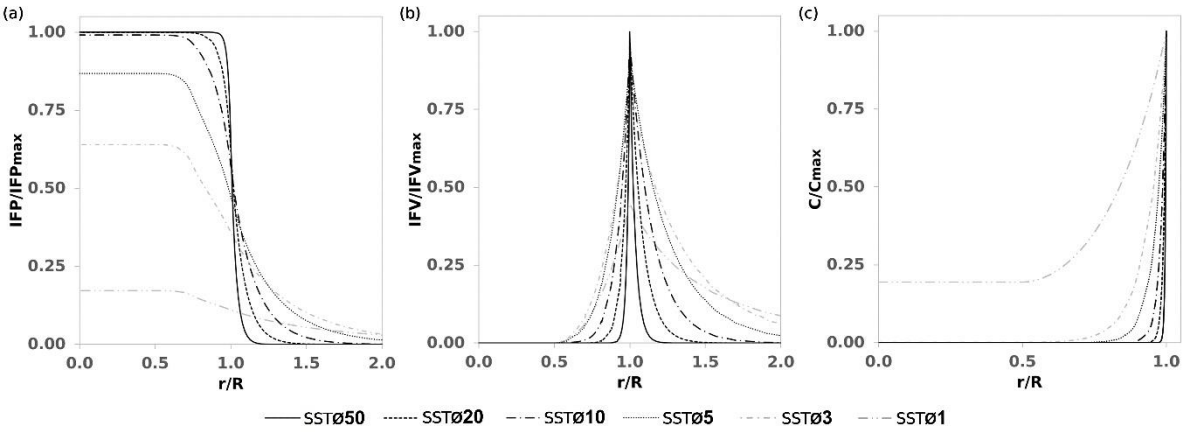

Fig 4. Dependency of IFP, IFV and drug penetration on the tumor size for the SST category (alymphatic and n_r=0.50). The 1 in the horizontal axis marks the interface between tumor and normal tissue.

In contrast with spherical tumors, the IFP for SET geometries (Fig. 5a,d) varies in the central region of the tumor due to the necrotic core with the maximum IFP located outside the necrotic core, in the hypoxic region, mainly due to the imbalance of the volume of interstitial fluid source (Fig. 5a). Moreover, while the IFP in the necrotic core is lower on the long axis, the IFP on the short axis is higher within the necrotic core. In all cases, the location of IFP50% is in the vicinity of tumor surface, inside tumor for the SETØ3, SETØ5 and SETØ10 and outside for the rest. On the short axis, however, the IFP50% was located outside the tumors in all cases. The results also demonstrated that the necrotic core effect on IFP diminishes for large tumors (Ø > 10 mm). Similar to SST group, the maximum IFV is at the tumor surface (Fig. 5b,e). However, none of the SET cases reached the highest IFV seen in the spherical tumors despite having similar volumes. Surprisingly, on the long axis, the highest IFV was seen in SETØ10 (98 nm/s) and then SETØ20 (94 nm/s) and not in the largest tumor (SETØ50; 88 nm/s) as it was in SST category. On the short axis, the highest IFV values were sorted with respect to the tumor size. However, the IFV profiles were heterogenous, for instance the SETØ3 had the highest IFV on both axes among all other SETs where r/R was between 0.7 and 0.9. Unlike the IFV in SST group, an active outwards flow exists inside the necrotic core when Ø < 10 mm. Moreover, a local increase in IFV was illustrated in SETØ1 to SETØ5 close to the surface of the necrotic core (Fig. 5b).

In the SET category, the two smallest tumors (SETØ1 and SETØ3) had a non-zero concentration on both long and short axes (Fig. 5 c,f). Also, on the long axis (Fig. 5c) the concentration profile is subject to change near the border of necrotic core from decreasing to increasing. One explanation could be that the decrease in outward flow near the necrotic core, provides the opportunity of less hindering flow against drug transport. Comparing the concentration profiles on long and short axes, the PDI is generally higher on the short axes ranging between 2% to 32% for SETØ50 to SETØ3, respectively. It was also determined that having similar conditions the penetration was deeper in SET category compared with the SST category. For instance, SSTØ5 had PDI of 13%, while the similar in size SETØ5 had PDI as high as 19%. Even comparing the concentration at a similar distance from the surface of the tumor, SET tumors had higher values. For instance, the concentration 1 mm deep in SETØ10 is two times larger than the same location in SSTØ10.

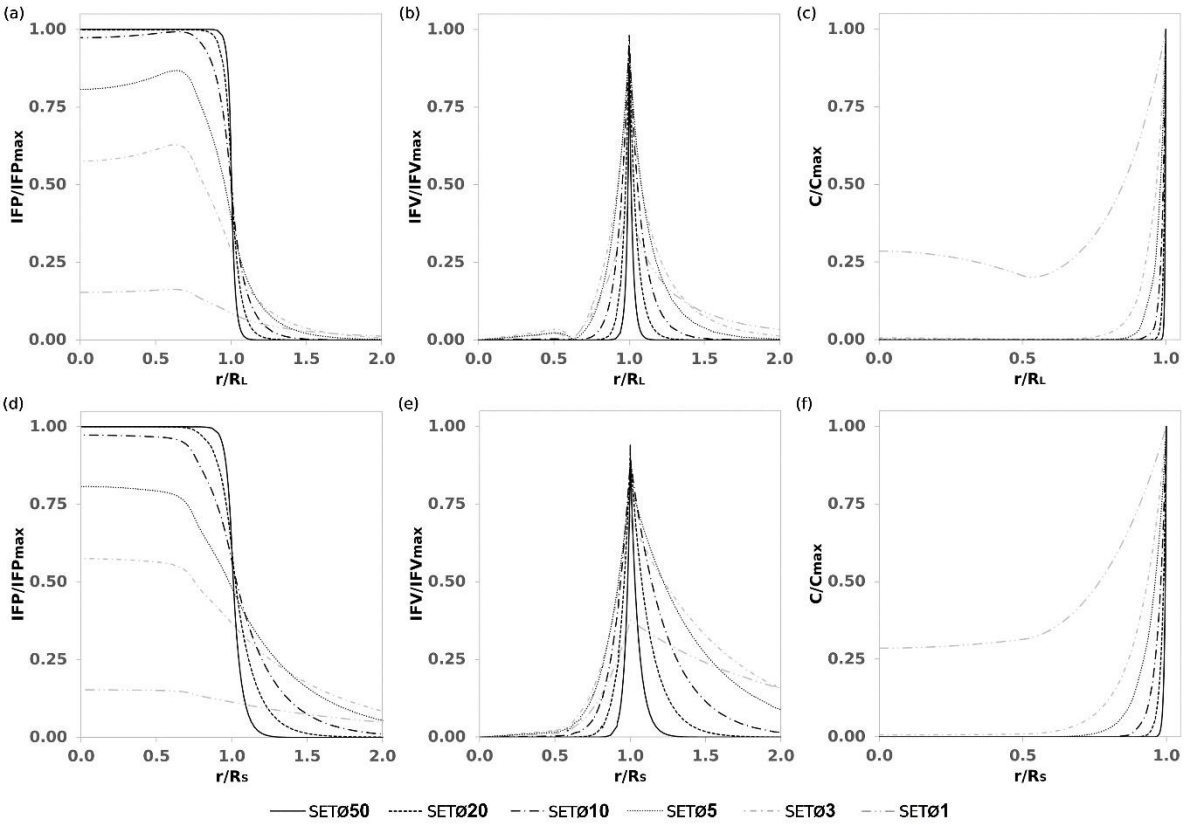

Fig 5. Dependency of IFP, IFV and drug penetration on the tumor size in SET category. **(a-c)** IFP, IFV and drug concentration on the long axis. **(d-f)** IFP, IFV and drug concentration on the short axis. The 1 in the horizontal axis marks the interface of tumor and normal tissue.

Also for the AET geometries, IFP does not correlate with the size in very large tumors (Fig. 6a,d). Moreover, when Ø < 50 mm, the IFP profile is not symmetric, and the highest IFP occurs in the half with lower necrosis (negative horizontal axis). The IFP drop also has a different trend in each AET, in which, on the long axis, the IFP50% was located inside tumors for the three small tumors. However, the location of IFP50% was not similar for larger tumors on the different halves. On the low necrosis side (negative axis), the point of IFP50% almost was on the surface of the tumor in AETØ10, AETØ20 and AETØ50, however, the same point was clearly outside the tumors on the positive axis. On the short axis, the IFP50% happened outside tumor in all cases. Having the highest IFV on the furthest distance from the necrotic core (negative axes; Fig. 6 b,e), except for AETØ20 and AETØ50, a non-zero IFV was detected all over the tumor. Surprisingly, the highest IFV in the largest tumor (AETØ50) was lower than all other AETs, and only reached a value about 50% of the maximum IFV (0.1 µm/s). Also, a less-steep IFV profile was observed outside the tumor on the short axis of all AETs (Fig. 6e). Similar to SST and SET groups, the opposing interstitial flow at the outside of the tumor was stronger in smaller tumors.

As a consequence of the heterogenous IFV in AETs, the penetration depth of the drug was also varying on the both axes (Fig. 6c,f), in which the penetration depth was shallower on the negative axis. Drug concentration in AETØ1 was significantly higher than the IC50 threshold on both axes. The concentration values in AETØ3 had a noticeable amount as well, having the PDI of 47% and 68% on the long and short axes, respectively. The largest AET illustrated the shallowest penetration with only about 2%. Generally, the penetration is deeper on the longer axis, where for instance in AETØ10 the penetration depth on the long axis is 5% more than the penetration on the short axis.

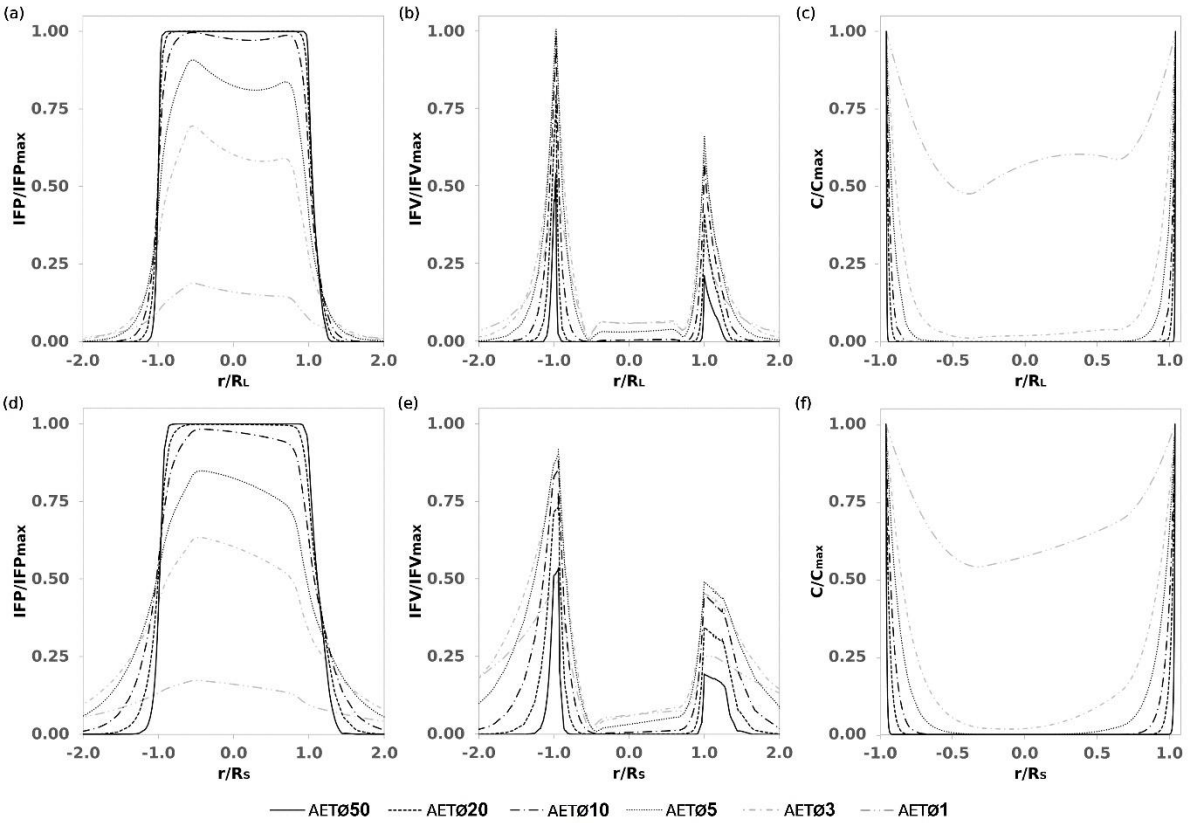

Fig 6. Dependency of IFP, IFV and drug penetration on the tumor size in AET category. **(a-c)** IFP, IFV and drug concentration on the long axis. **(d-f)** IFP, IFV and drug concentration on the short axis. The 1 in the horizontal axis marks the interface of tumor and normal tissue.

3b. Necrotic core size

Fig. 7, illustrates the effect of presence of a necrotic core on a small (D=5mm; white zone) and a large tumor (D=50mm; gray zone) in SST category (Fig. 7). While the presence of a necrotic core barely affects the tumor perfusion (IFP and IFV profiles) in the large tumor, it can drastically alter small tumor perfusion (Fig. 7a-b). Also, the decrease in IFP and IFV intensified with respect to the necrotic core size in the small tumor, in which IFP in the small tumor with n_r=75% demonstrated a 33% decrease in IFP compared with the same tumor without a necrotic core. The location of IFP50% was also on the tumor surface in both the large and small tumors for all n_r ratios. No clear effect on the IFV profile was observed in the presence of a necrotic core in large tumors.. In the small tumor, the effect of a large necrotic core is not only limited to the core itself, but it can also decrease the IFV outside the tumor (Fig. 7b). However, the degree of IFV alteration is not noticeable close to the periphery of the tumor. According to Fig. 7c, the change of IFP as well as IFV due to necrotic core presence did not contribute in the same way to drug delivery for both large and small tumors, in which no clear enhancement of drug concentration was detected.

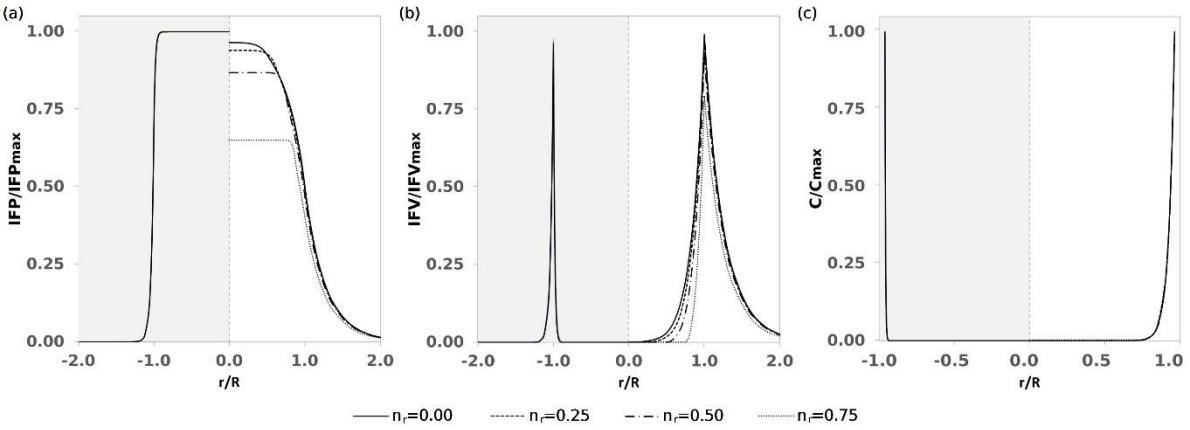

Fig 7. Effect of necrotic core on the **(a)** IFP, **(b)** IFV and **(c)** drug penetration in the SST category in a large tumor (D=50 mm; grey zone) and a small tumor (D=5 mm; white zone).

In the SET category, the generation of a necrotic region decreases the IFP in the small tumor, but not in the large tumor (Fig. 8a,e). Having a necrotic core with a n_r of 75% in the small tumor can cause a decrease of 28% and 38% in the highest IFP on long and short axes, respectively. This decrease is even more profound on the long axis and on the center of the tumor, where the IFP (solid line at r/R=0) reduction is about 40%. It is also worth mentioning that the IFP profile is not always subject to a reduction due to a necrotic core, but as depicted in Fig. 8a,d the IFP of the small SET with an n_r of 25% or 50% is higher than IFP in the non-necrotic tumor where r/R is between 0.5 and 0.7.

Similar insensitivity to necrotic core was observed in the large SET, however, the analysis of IFP50% in the small tumor revealed that the presence of a necrotic core pushed the IFP50% location outwards in all cases. In contrast with spherical tumors, where the presence of the necrotic core did not contribute in the generation of IFV inside the core, results showed (Fig. 8b,e) a non-zero IFV inside the core in SETs. On the short axis, a smooth increase in IFV was observed towards the tumor surface, however, a local gradient was also detected close to the necrotic core border on the long axis (Fig. 8b).

The interaction of necrotic core with the drug delivery was also presented in Fig. 8c,f. Despite the fact that the general trend demonstrated the infectivity of necrotic core on drug penetration in spherical tumors, results on SETs, highlight a clear impact on the penetration profile due to a necrotic core with a n_r of 75%. Surprisingly, on the long axis, a turning point exists close to the border of the hypoxic region, where the trend of concentration profile changed from decreasing to increasing. Results showed that the PDI of the small tumor with a n_r of 75% can increase about 10% on both axes compared with a non-necrotic tumor.

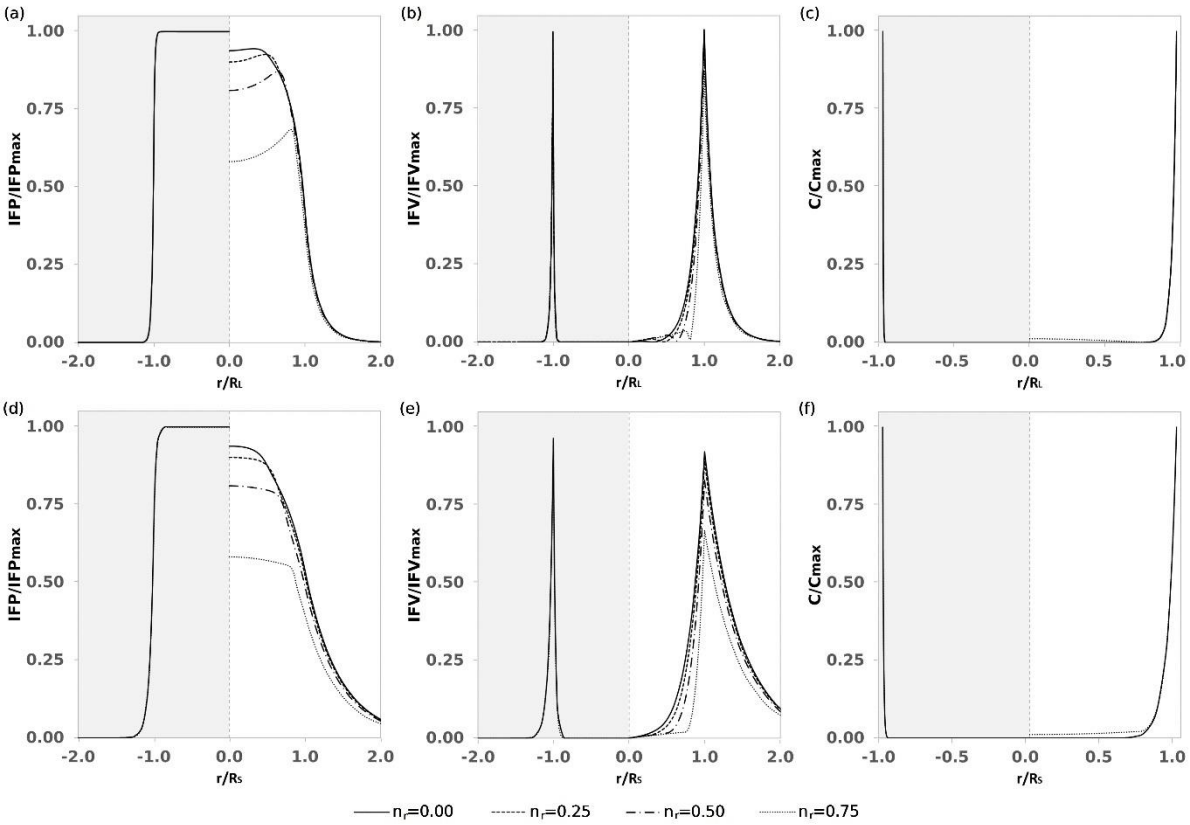

Fig 8. Effect of necrotic core on the **(a, d)** IFP, **(b, e)** IFV and **(c, f)** drug penetration in the SET category on **(a-c)** long and **(d-f)** short axes in a large tumor (D=50 mm; grey zone) and a small tumor (D=5 mm; white zone).

The tumor perfusion of AETs in the presence of a necrotic core was investigated in Fig. 9. While there was not any clear effect of necrotic core on the IFP in large tumors in the symmetric tumors (i.e. SST and SET categories), the IFP is affected by even the smallest necrotic core (i.e. n_r=0.25) in AETs (Fig. 9a,g). Results illustrated that although the highest IFP in each large AET was not affected by a necrotic core, the IFP profile reacts in the response to existence of a necrotic core. However, the impact is only limited to the outer region of the tumor, in which the IFP alternation inside the tumor only happens in the less necrotic region (negative axis). IFP results in the small tumor (Fig. 9d,j) also revealed the dependency of IFP heterogeneity on the size of the necrotic core.

Regarding the IFP50% in AETs with necrotic core, except with n_r of 75%, the location of IFP50% fell out of the tumor. Even in the case of the n_r of 75%, only about 10% of the IFP values inside tumor were below the criteria. A noticeable heterogeneity was detected in the IFV profiles, in which while the presence of a necrotic core generally increased the IFV on tumor surface of less necrotic region (i.e r/R=-1), the corresponding value on the other side (i.e r/R=1) decreased (Fig. 9b,e,h,k). In the large tumor and on the both axes (Fig. 9b,h), the highest IFV seen in the tumor does not go far beyond 50% of the maximum IFV detected in symmetric tumors. Also, the IFV values of the large tumor in the less necrotic region (negative axis) and close to the tumor surface (r/R=-1) were twice as high as the IFV values in the corresponding positive axis. In the small tumor, the difference between the two sides can get as high as 70% (when n_r=75%), but the diversity of IFV values on tumor surface is lower compared to the large tumor. Considerable non-zero IFV was also detected inside the small tumor, specially inside the necrotic core (Fig. 9e,k).

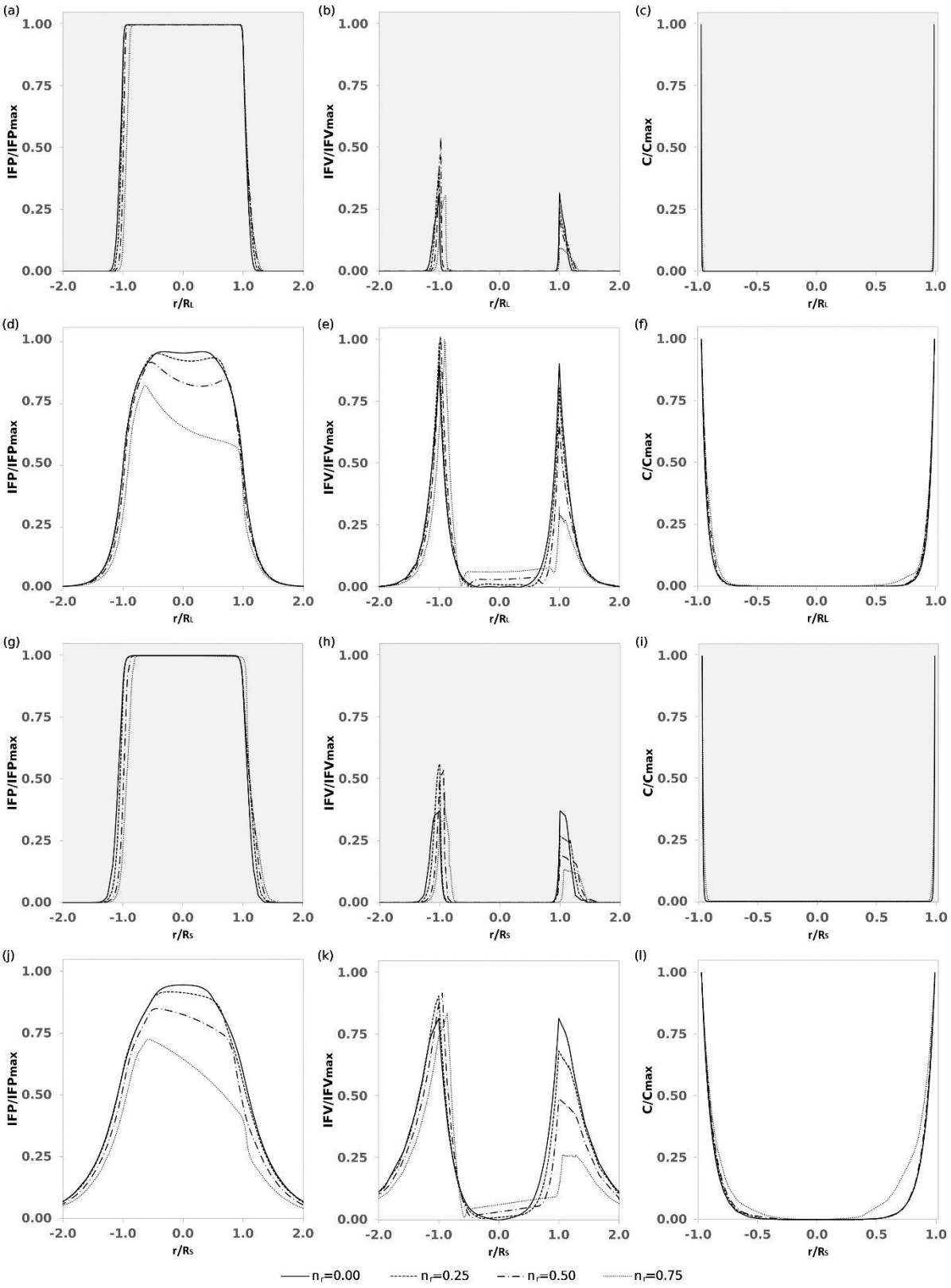

Fig 9. Effect of necrotic core on the **(a, d, g, j)** IFP, **(b, e, h, k)** IFV and **(c, f, i, l)** drug penetration in the AET category on **(a-f)** long and **(g-l)** short axes in a large tumor (D=50 mm; grey zone) and a small tumor (D=5 mm; white zone).

Despite the profound impacts on IFP as well as IFV due to necrosis in the large tumor, the penetration of the drug was not affected clearly, except in case of the large necrotic core (Fig. 9c,i). Results showed

that, the PDI of the large tumor with n_r of 0.75 got doubled compared with the PDI of the large tumor without a necrotic core or with a smaller core (i.e. n_r of 0.25 or 0.5). On the other hand, results demonstrated the significant role of necrotic core on the drug penetration in the small tumor (Fig. 9f,l). Clearly, the small tumor with a large core can change the penetration profile in the inner region of the tumor. While the PDI of the non-necrotic small tumor was 16% (on the LA; 30% on SA), the PDI of the small tumor with an n_r of 0.75 was 22% (on the LA; 45% on SA). Results showed that even in case of a smaller necrotic core, the concentration of the drug enhanced especially in the low necrosis region (negative axis).

3c. Presence of lymphatic vessels

In all three geometrical categories (SST, SET, and AET), the presence of lymphatic drainage at the outer layers of the tumor mainly resulted in a slight reduction of IFP. The reduction in IFP was more noticeable in the central regions of small tumors, such as necrotic and intermediate regions, whereas in large tumors, the reduction in IFP was limited to the peripheral region as shown in Fig. S1-S3. Minimal effects of lymphatic drainage were also observed on IFV in some cases; however, no correlation was found to exist between lymphatic drainage and drug penetration (more details in the supplementary material).

4. Discussion

The current computational model of interstitial fluid flow in solid tumors, to our knowledge, is the first work to account for the heterogeneity of solid tumors properties including interstitium hydraulic conductivity, vascular permeability and lymphatic drainage. Furthermore, within this framework, the effects of geometrical features of tumors such as tumor and necrotic core size, shape and configuration were also investigated.

The observed uneven distribution and suboptimal penetration efficacy of therapeutic agents are the sign of heterogeneity of biophysical properties of solid tumor [64], namely blood vessel permeability, hydraulic conductivity of tumor tissue as well as lymphatic drainage. In contrast, the common trend in the computational models of interstitial fluid flow with homogeneous parameters can lead to oversimplification and reduced accuracy. Heterogeneous modeling allows for a more nuanced and realistic representation of the system being modeled.

The novelties of modeling interstitial fluid pressure and drug transport with realistic heterogeneous parameters include (i) a better representation of spatial variations (heterogeneity) in biophysical properties, (ii) improved accuracy in predictions (i.e. IFP, IFV, drug concentration), and (iii) a more robust modeling approach for tumor perfusion and drug penetration. More specifically, it was shown that the biophysical characteristics of solid tumors (i.e. blood and lymph vessels as well as necrotic core) can largely alter the interstitial fluid flow (Fig. 3d-e). Contrarily, most of the published articles have commonly simplified the prescription of tumor material properties by considering only a few distinct zones [30], such as the necrotic core and viable region, while overlooking the transitions occurring within each zone (depicted by the orange dashed line in Fig. 3d-e). Additionally, while image-based models such as [23, 32] offer a more realistic approach, the parametric design adopted in the present study enables more detailed investigations. Moreover, the partial presence of lymphatic drainage within solid tumors has been largely neglected, leading to an unrealistic abrupt transition from an alymphatic zone of tumor to a fully functional lymphatic region at the tumor border [21, 27].

To this date, except for a few studies, a single unique permeability value was typically used in all simulations on tumor interstitial flow, neglecting the proven heterogeneity of tumor biomechanical

properties, such as hydraulic conductivity [37, 44, 65]. In our current study, we suggest a profile for interstitium permeability that corresponds with experimental observations [37], generally assuming lower values inside the tumor compared to the surrounding normal tissue. We previously found that *K* values change the course of the IFP profile [37, 38]. Based on the current study, we also suggest that the maximum value of IFP is directly related to the permeability of blood vessels as well as the lack of normal functioning lymphatic vessels.

To our knowledge, this is the first theoretical model that embeds the heterogeneity of blood capillaries of solid tumors. Our findings showed that the permeability profile lowers the IFP within the tumor compared to predictions of previous investigations [15, 16, 21, 27, 30, 46], for which constant vascular permeability values were higher. However, this effect is limited to some regions of the tumor (e.g. necrotic core and viable region) depending on its size and shape.

The selection of the SST as a starting point allowed for comparison with the state-of-the-art literature [15-17, 27, 30, 34, 35, 66-72], while implementing SET was based on the observations in numerous cancer cases [27]. Additionally, the AET category served as an example of the observed asymmetry in solid tumors [23, 32]. In contrast, the majority of previous studies were focused on one single geometry [21], or in the case of investigating several geometries, they were all perfectly symmetric [21, 27] or isometric [33]. While the shape and size of the tumor can be great factors affecting tumor perfusion, our results suggest that the effect on large tumors (Ø > 50 mm) is negligible. For smaller tumors, as shown in Fig. 5-6, the popular prediction of an IFP plateau in the center of the tumor is not accurate, when having non-spherical tumors. Unlike many previous works' predictions [16, 21, 30], for a non-spherical tumor, the IFV can get to a non-zero value inside the necrotic core, opposing the convective transport of the drug.

It was found that the IFP correlates with the tumor size independent of the tumor shape and configuration, except when the tumor volume is larger than 65 cm^3. Moreover, the sensitivity of the maximum IFP to tumor size decreases with increasing tumor size. For instance, the highest IFP seen in SSTs, SETs and AETs larger than 1 cm^3 were similar, although the profiles of IFP were diverse. On the other hand, the IFV profiles were not necessarily correlated with the tumor size.

As mentioned, the Peclet number can provide a measure to evaluate the mechanisms of drug transport, weighing the convection over diffusion. An analysis showed that in all cases the Peclet number was lower than 0.002, indicating that diffusion has a major role in drug transport into the interstitium. This caused a size-dependent concentration profile in all symmetric cases (i.e. SSTs and SETs), in which - despite the small differences - the absolute penetration depths were almost similar. In AETs, the linear correlation between tumor size and penetration depth also holds when the tumor was larger than 5 cm^3. In all smaller cases (i.e. AETØ5, AETØ3 and AETØ1), the penetration rim had a varying thickness, with a deeper penetration on the less necrotic side.

Looking at the penetration profiles of the smallest non-spherical tumors, an increasing gradient can be seen in the inner regions (Fig. 5c & 6c). First, regarding the lower opposing flow in these tumors, the diffusion is less hindered, causing an accumulation of the drug in the tumor center. The other important factor is the shape of the tumor, which provides a shorter pathway for the diffusive transport. This phenomenon has also been described by Jain and Baxter [73] claiming that the accumulation of the drug in the center can act as a secondary reservoir for the drug release to the outer region in considerably slow processes.

Generally, the presence of a necrotic core inside solid tumors lowers the IFP since it reduces the volumetric source of interstitial flow generation. In contrast to previous findings where the effect of a necrotic core on IFP was limited to large cores (over 80% of the tumor volume) [15, 16, 30, 46, 74], our findings suggest that a core with a tumor volume of only 25% can alter the IFP profile. In addition, [30, 75], we showed that in case of asymmetric tumor configurations, the IFP profile can be dependent on the necrotic core size. The sensitivity of IFV values to necrotic core size was noticeably higher in the smaller tumors. As a new perspective, we showed that although a larger necrotic core lowers the IFP more, IFP values in some regions at the tumor periphery can still be higher in tumors with larger necrotic core. Results also showed that the generation of a necrotic core can enhance the penetration of the drug, depending on the size and shape of the necrotic core as well as the tumor, except in spherical tumors.

The results proved the minimal effect of a newly-grown lymphatic network (due to possible lymphangiogenesis process) on the IFP profile, having a limited lowering effect. Moreover, the IFV profile was even altered less. Accordingly, our findings showed that the presence of lymphatic vessels does not enhance the drug delivery. This claim was previously corroborated by Baxter and Jain [15], where they claimed that the drug concentration may even significantly reduce as fluid and solutes are reabsorbed from the tumor interstitium by the lymphatic vessels. Our findings are in line with previous studies, where it has been established that the amount of fluid infiltration from capillaries (J_v) is much greater compared to the lymphatic drainage (J_l) [76-78].

For data, model, and result validity, the computational model inputs (parameters and profiles) were precisely prescribed based on current knowledge, including our ex-vivo study on tumor tissue hydraulic conductivity [38]. Model output was compared with published literature, with a maximum IFP value (IFPmax) of 11.5 mmHg, consistent with previous experimental observations [79-81].

A number of simplifications and assumptions were made when developing the models. The boundary conditions and geometries used in our simulations were idealized, which cannot fully recreate the realistic case. Additionally, despite the attempt to profile the biophysical properties accurately, more authentic profiling is possible with usage of patient-specific data, which will be explored in our future works. In this context, combining computational modeling with quantitative imaging data, like dynamic contrast-enhanced MRI (DCE-MRI), as well as in-vitro models can fill the gap of personalized models of tumor perfusion and drug delivery.

5. Conclusion

Interstitial fluid flow plays an important role in the treatment of solid tumors regarding drug delivery. Our results demonstrated that depending on tumor size and shape, the presence of a necrotic core can noticeably change the IFP profile. Also, even impaired lymph drainage at the periphery of the tumor decreases the IFP. The IFP strongly correlates with the size of the tumor for small tumors. This study highlights the importance of using realistic tumor geometries and accounting for heterogeneous tumor properties such as hydraulic conductivity and tumor permeability in the development of personalized computational oncology.

6. Acknowledgements

This work was funded by grants from Stichting tegen Kanker (project 2018-104) and the Research Foundation – Flanders (FWO, project number 3G020919).

References

1. Sung, H., et al., *Global cancer statistics 2020: GLOBOCAN estimates of incidence and mortality worldwide for 36 cancers in 185 countries.* CA: a cancer journal for clinicians, 2021. **71**(3): p. 209-249.
2. Junghans, R.P., *The challenges of solid tumor for designer CAR-T therapies: a 25-year perspective.* Cancer gene therapy, 2017. **24**(3): p. 89-99.
3. Salavati, H., et al., *Interstitial fluid pressure as an emerging biomarker in solid tumors.* Biochimica et Biophysica Acta (BBA)-Reviews on Cancer, 2022: p. 188792.
4. Yao, N., et al., *Primary tumor removal improves the prognosis in patients with stage IV breast cancer: A population-based study (cohort study).* International Journal of Surgery, 2020. **83**: p. 109-114.
5. Tohme, S., R.L. Simmons, and A. Tsung, *Surgery for cancer: a trigger for metastases.* Cancer research, 2017. **77**(7): p. 1548-1552.
6. Vasir, J.K. and V. Labhasetwar, *Targeted drug delivery in cancer therapy.* Technology in cancer research & treatment, 2005. **4**(4): p. 363-374.
7. Jang, S.H., et al., *Drug delivery and transport to solid tumors.* Pharmaceutical research, 2003. **20**(9): p. 1337-1350.
8. Jain, R.K., *Determinants of tumor blood flow: a review.* Cancer research, 1988. **48**(10): p. 2641-2658.
9. Nagy, J., et al., *Why are tumour blood vessels abnormal and why is it important to know?* British journal of cancer, 2009. **100**(6): p. 865-869.
10. Gillies, R.J., et al., *Causes and effects of heterogeneous perfusion in tumors.* Neoplasia, 1999. **1**(3): p. 197-207.
11. Lunt, S.J., et al., *Interstitial fluid pressure in tumors: therapeutic barrier and biomarker of angiogenesis.* 2008.
12. Staudacher, A.H., V. Liapis, and M.P. Brown, *Therapeutic targeting of tumor hypoxia and necrosis with antibody α-radioconjugates.* Antibody Therapeutics, 2018. **1**(2): p. 55.
13. Emon, B., et al., *Biophysics of tumor microenvironment and cancer metastasis-a mini review.* Computational and Structural Biotechnology Journal, 2018. **16**: p. 279-287.
14. Zhan, W., M. Alamer, and X.Y. Xu, *Computational modelling of drug delivery to solid tumour: understanding the interplay between chemotherapeutics and biological system for optimised delivery systems.* Advanced Drug Delivery Reviews, 2018. **132**: p. 81-103.
15. Baxter, L.T. and R.K. Jain, *Transport of fluid and macromolecules in tumors. II. Role of heterogeneous perfusion and lymphatics.* Microvascular research, 1990. **40**(2): p. 246-263.
16. Baxter, L.T. and R.K. Jain, *Transport of fluid and macromolecules in tumors. I. Role of interstitial pressure and convection.* Microvascular research, 1989. **37**(1): p. 77-104.
17. Sarntinoranont, M., F. Rooney, and M. Ferrari, *Interstitial stress and fluid pressure within a growing tumor.* Annals of biomedical engineering, 2003. **31**(3): p. 327-335.
18. Pishko, G.L., et al., *Sensitivity analysis of an image-based solid tumor computational model with heterogeneous vasculature and porosity.* Annals of biomedical engineering, 2011. **39**(9): p. 2360.
19. Pishko, G.L., et al., *Role of convection and diffusion on DCE-MRI parameters in low leakiness KHT sarcomas.* Microvascular research, 2012. **84**(3): p. 306-313.
20. Zhao, J., H. Salmon, and M. Sarntinoranont, *Effect of heterogeneous vasculature on interstitial transport within a solid tumor.* Microvascular research, 2007. **73**(3): p. 224-236.
21. Sefidgar, M., et al., *Numerical modeling of drug delivery in a dynamic solid tumor microvasculature.* Microvascular research, 2015. **99**: p. 43-56.
22. Soltani, M. and P. Chen, *Numerical modeling of interstitial fluid flow coupled with blood flow through a remodeled solid tumor microvascular network.* PloS one, 2013. **8**(6): p. e67025.
23. Steuperaert, M., et al., *A 3D CFD model of the interstitial fluid pressure and drug distribution in heterogeneous tumor nodules during intraperitoneal chemotherapy.* Drug delivery, 2019. **26**(1): p. 404-415.

24. Milosevic, M.F., A.W. Fyles, and R.P. Hill, *The relationship between elevated interstitial fluid pressure and blood flow in tumors: a bioengineering analysis.* International Journal of Radiation Oncology* Biology* Physics, 1999. **43**(5): p. 1111-1123.
25. Milosevic, M., A. Fyles, and R. Hill, *Interstitial fluid pressure in cervical cancer: guide to targeted therapy.* American journal of clinical oncology, 2001. **24**(5): p. 516-521.
26. Tang, L., et al., *Computational modeling of 3D tumor growth and angiogenesis for chemotherapy evaluation.* PloS one, 2014. **9**(1): p. e83962.
27. Sefidgar, M., et al., *Effect of tumor shape, size, and tissue transport properties on drug delivery to solid tumors.* Journal of biological engineering, 2014. **8**(1): p. 1-13.
28. d'Esposito, A., et al., *Computational fluid dynamics with imaging of cleared tissue and of in vivo perfusion predicts drug uptake and treatment responses in tumours.* Nature Biomedical Engineering, 2018. **2**(10): p. 773-787.
29. Sweeney, P.W., et al., *Modelling the transport of fluid through heterogeneous, whole tumours in silico.* PLoS computational biology, 2019. **15**(6): p. e1006751.
30. Steuperaert, M., et al., *Mathematical modeling of intraperitoneal drug delivery: simulation of drug distribution in a single tumor nodule.* Drug delivery, 2017. **24**(1): p. 491-501.
31. Swinburne, N., et al., *Computational modeling of interstitial fluid pressure and velocity in non-small cell lung cancer brain metastases treated with stereotactic radiosurgery.* Frontiers in neurology, 2020. **11**: p. 402.
32. LoCastro, E., et al., *Computational modeling of interstitial fluid pressure and velocity in head and neck cancer based on dynamic contrast-enhanced magnetic resonance imaging: feasibility analysis.* Tomography, 2020. **6**(2): p. 129.
33. Moghadam, M.C., et al., *Numerical simulation of the tumor interstitial fluid transport: consideration of drug delivery mechanism.* Microvascular Research, 2015. **101**: p. 62-71.
34. Welter, M. and H. Rieger, *Interstitial fluid flow and drug delivery in vascularized tumors: a computational model.* PloS one, 2013. **8**(8): p. e70395.
35. Pusenjak, J. and D. Miklavcic, *Modeling of interstitial fluid pressure in solid tumor.* Simulation Practice and Theory, 2000. **8**(1-2): p. 17-24.
36. Netti, P.A., et al., *Role of extracellular matrix assembly in interstitial transport in solid tumors.* Cancer research, 2000. **60**(9): p. 2497-2503.
37. Salavati, H., et al., *Interstitial Fluid Pressure and Hydraulic Conductivity in Solid Tumors: Introducing an In-Vitro Method for Measuring the Hydraulic Conductivity of Tumor Tissue.* European Journal of Surgical Oncology, 2022. **48**(2): p. e145-e146.
38. Salavati, H., et al., *Hydraulic Conductivity of Human Cancer Tissue: a Hybrid study* Bioengineering and Translational Medicine 2023. **Under review**.
39. Salavati, H., et al. *The effect of a necrotic core on the interstitial fluid pressure in solid tumors*. in *17th International Symposium on Computer Methods in Biomechanics and Biomedical Engineering and 5th Conference on Imaging and Visualization*. 2021.
40. Salavati, H., et al. *Resistance to intraperitoneal drug delivery and heterogeneity of peritoneal metastasis: the role of hydraulic conductivity*. in *2nd Congress of the International Societyfor the Study of Pleura and Peritoneum*. 2021.
41. Salavati, H., et al., *Connecting the macro-and micro-scale properties in human solid tumors: hydraulic conductivity.* European Journal of Surgical Oncology, 2023. **49**(2): p. e59-e60.
42. Salavati, H., et al. *Influence of the peritoneal metastatic microenvironment on interstitial permeability*. in *3rd Congress of the International Society for the Study of Pleura and Peritoneum (ISSPP)*. 2022.
43. Salavati, H., et al. *Integrating DCE-MRI and IVIM-DWI in a computational simulation of interstitial fluid pressure in a pancreatic tumor*. in *15th Annual Meeting of the ISMRM Benelux Chapter*. 2023.
44. Liu, L. and M. Schlesinger, *Interstitial hydraulic conductivity and interstitial fluid pressure for avascular or poorly vascularized tumors.* Journal of Theoretical Biology, 2015. **380**: p. 1-8.

45. Chatterjee, K., et al., *Utilizing Dynamic Contrast-Enhanced Magnetic Resonance Imaging (DCE-MRI) to Analyze Interstitial Fluid Flow and Transport in Glioblastoma and the Surrounding Parenchyma in Human Patients.* Pharmaceutics, 2021. **13**(2): p. 212.
46. Soltani, M. and P. Chen, *Effect of tumor shape and size on drug delivery to solid tumors.* Journal of biological engineering, 2012. **6**(1): p. 1-15.
47. Islam, M.T., et al., *An analytical model of tumors with higher permeability than surrounding tissues for ultrasound elastography imaging.* Journal of Engineering and Science in Medical Diagnostics and Therapy, 2018. **1**(3).
48. Levick, J., *Flow through interstitium and other fibrous matrices.* Quarterly Journal of Experimental Physiology: Translation and Integration, 1987. **72**(4): p. 409-437.
49. Jain, R.K., *Transport of molecules in the tumor interstitium: a review.* Cancer research, 1987. **47**(12): p. 3039-3051.
50. Swabb, E.A., J. Wei, and P.M. Gullino, *Diffusion and convection in normal and neoplastic tissues.* Cancer research, 1974. **34**(10): p. 2814-2822.
51. Wei, J., et al., *Roles of proteoglycans and glycosaminoglycans in cancer development and progression.* International journal of molecular sciences, 2020. **21**(17): p. 5983.
52. Xu, S., et al., *The role of collagen in cancer: from bench to bedside.* Journal of translational medicine, 2019. **17**(1): p. 1-22.
53. Kedem, O. and A. Katchalsky, *Thermodynamic analysis of the permeability of biological membranes to non-electrolytes.* Biochimica et biophysica Acta, 1958. **27**: p. 229-246.
54. Zhang, L., et al., *A feasible method of angiogenesis assessment in gastric cancer using 3D microvessel density.* Stem cells international, 2018. **2018**.
55. Mussurakis, S., P. Gibbs, and A. Horsman, *Peripheral enhancement and spatial contrast uptake heterogeneity of primary breast tumours: quantitative assessment with dynamic MRI.* Journal of computer assisted tomography, 1998. **22**(1): p. 35-46.
56. Buadu, L.D., et al., *Breast lesions: correlation of contrast medium enhancement patterns on MR images with histopathologic findings and tumor angiogenesis.* Radiology, 1996. **200**(3): p. 639-649.
57. Bottaro, A. and T. Ansaldi, *On the infusion of a therapeutic agent into a solid tumor modeled as a poroelastic medium.* 2012.
58. Leunig, M., et al., *Interstitial fluid pressure in solid tumors following hyperthermia: possible correlation with therapeutic response.* Cancer research, 1992. **52**(2): p. 487-490.
59. Rasouli, S.S., I.W. Jolma, and H.A. Friis, *Impact of spatially varying hydraulic conductivities on tumor interstitial fluid pressure distribution.* Informatics in Medicine Unlocked, 2019. **16**: p. 100175.
60. Alitalo, K., T. Tammela, and T.V. Petrova, *Lymphangiogenesis in development and human disease.* Nature, 2005. **438**(7070): p. 946-953.
61. Thiele, W. and J.P. Sleeman, *Tumor-induced lymphangiogenesis: a target for cancer therapy?* Journal of biotechnology, 2006. **124**(1): p. 224-241.
62. Stacker, S.A., et al., *VEGF-D promotes the metastatic spread of tumor cells via the lymphatics.* Nature medicine, 2001. **7**(2): p. 186-191.
63. Yao, W., Y. Li, and G. Ding, *Interstitial fluid flow: the mechanical environment of cells and foundation of meridians.* Evidence-Based Complementary and Alternative Medicine, 2012. **2012**.
64. Miao, L., C.M. Lin, and L. Huang, *Stromal barriers and strategies for the delivery of nanomedicine to desmoplastic tumors.* Journal of Controlled Release, 2015. **219**: p. 192-204.
65. Hormuth, D.A., A.M. Jarrett, and T.E. Yankeelov, *Forecasting tumor and vasculature response dynamics to radiation therapy via image based mathematical modeling.* Radiation Oncology, 2020. **15**(1): p. 1-14.
66. Boucher, Y., L.T. Baxter, and R.K. Jain, *Interstitial pressure gradients in tissue-isolated and subcutaneous tumors: implications for therapy.* Cancer research, 1990. **50**(15): p. 4478-4484.

67. Netti, P.A., et al., *Time-dependent behavior of interstitial fluid pressure in solid tumors: implications for drug delivery.* Cancer Research, 1995. **55**(22): p. 5451-5458.
68. Milosevic, M., et al., *Interstitial permeability and elasticity in human cervix cancer.* Microvascular research, 2008. **75**(3): p. 381-390.
69. Liu, L., et al., *Phenomenological model of interstitial fluid pressure in a solid tumor.* Physical Review E, 2011. **84**(2): p. 021919.
70. Burazin, A., et al., *A poroelasticity theory approach to study the mechanisms leading to elevated interstitial fluid pressure in solid tumours.* Bulletin of mathematical biology, 2018. **80**(5): p. 1172-1194.
71. Zheng, Y., Y. Jiang, and Y. Cao, *Effects of interstitial fluid pressure on shear wave elastography of solid tumors.* Extreme Mechanics Letters, 2021. **47**: p. 101366.
72. Kiani Shahvandi, M., et al., *Spatiotemporal multi-scale modeling of radiopharmaceutical distributions in vascularized solid tumors.* Scientific reports, 2022. **12**(1): p. 14582.
73. Jain, R.K. and L.T. Baxter, *Mechanisms of heterogeneous distribution of monoclonal antibodies and other macromolecules in tumors: significance of elevated interstitial pressure.* Cancer research, 1988. **48**(24_Part_1): p. 7022-7032.
74. Sefidgar, M., E. Bashooki, and P. Shojaee, *Numerical simulation of the effect of necrosis area in systemic delivery of magnetic nanoparticles in hyperthermia cancer treatment.* Journal of thermal biology, 2020. **94**: p. 102742.
75. Rezaeian, M., M. Soltani, and F. Moradi Kashkooli. *On the modeling of drug delivery to solid tumors; Computational viewpoint*. in *International Conference on Applied Mathematics, Modeling and Computational Science*. 2019. Springer.
76. Sevick, E.M. and R.K. Jain, *Blood flow and venous pH of tissue-isolated Walker 256 carcinoma during hyperglycemia.* Cancer research, 1988. **48**(5): p. 1201-1207.
77. Vaupel, P., et al., *Blood flow, oxygen consumption, and tissue oxygenation of human breast cancer xenografts in nude rats.* Cancer research, 1987. **47**(13): p. 3496-3503.
78. Butler, T.P., F.H. Grantham, and P.M. Gullino, *Bulk transfer of fluid in the interstitial compartment of mammary tumors.* Cancer research, 1975. **35**(11): p. 3084-3088.
79. Gutmann, R., et al., *Interstitial hypertension in head and neck tumors in patients: correlation with tumor size.* Cancer research, 1992. **52**(7): p. 1993-1995.
80. Willett, C.G., et al., *Direct evidence that the VEGF-specific antibody bevacizumab has antivascular effects in human rectal cancer.* Nature medicine, 2004. **10**(2): p. 145-147.
81. Nielsen, T., et al., *Non-invasive imaging of combretastatin activity in two tumor models: Association with invasive estimates.* Acta Oncologica, 2010. **49**(7): p. 906-913.

Supplementary materials

Results in Fig. S1 show that the presence of partially active lymph drainage in SSTs at the periphery region can affect the small and large tumors in two different ways. While in the large tumors the IFP decreased in the periphery region (Fig. S1a; gray zone), the IFP reduction in the small tumors was more noticeable in central regions (i.e. necrotic and intermediate regions). The extent of plateau IFP was comparable between different cases in small tumors, however, the extent of plateau was decreasing with increasing lymph drainage in large tumors. Also, the sensitivity of IFP to lymph vessels is higher in the large tumor, where a highly practical lymphatic drainage (dotted line) can cause a IFP decrease of 16% in the large tumor and only 2% in the small tumor.

The location of IFP50% was outside of the tumor in both the large and small tumors independent on the presence of lymph drainage, resulting in a uniform IFP gradient. Fig. S1b illustrated the IFV profiles

in the large and the small tumor in presence of lymphatic vessels. In general, no important difference was observed in the small tumor (Fig. S1b; white zone), except that the magnitude of highest IFV was decreased in respect to the potency of drainage, for instance about 8% when having a high drainage rate. In the large tumor, the decrease in the highest IFV is more noticeable, where existing a high lymph drainage profile reduced the IFV about 17%. Furthermore, the extent of the no-flow region (i.e. IFV = 0) was reduced in respect to the lymphatic drainage capacity, and close to the border of the tumor. Accordingly, while the no-flow region extended to about 90% of the tumor having no lymph drainage, the no-flow region was limited to 74%, 77% and 86% for high, medium and low lymphatic drainage, respectively. However, having almost same IFV profiles in all cases, an unified opposing convective flow was generated inside the tumors. Fig. S1c showed that the effect of lymphatic drainage is negligible on the penetration profile, in both the large and small SSTs.

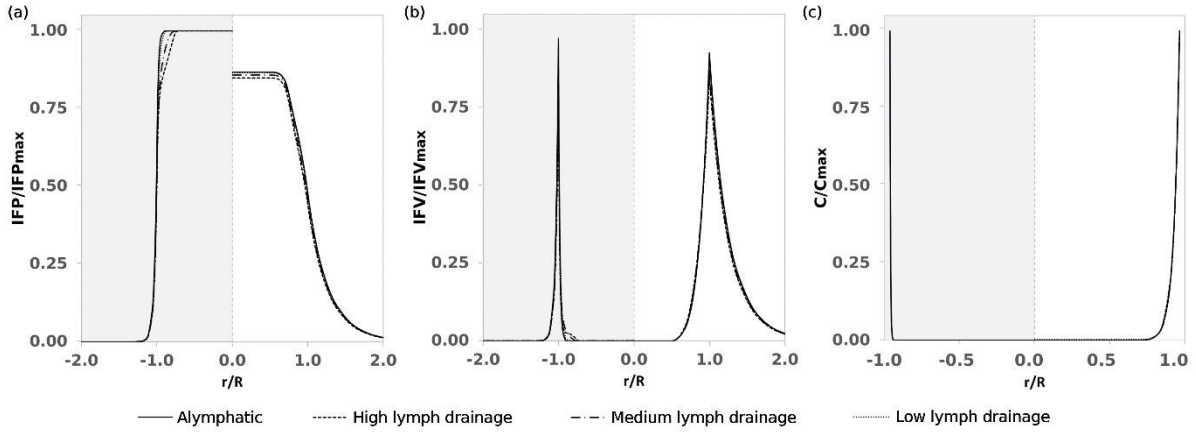

Fig S1. Effect of presence of lymphatic drainage on the (a) IFP and (b) IFV and (c) drug penetration in SST category in a large tumor (D=50 mm; grey zone) and a small tumor (D=5 mm; white zone).

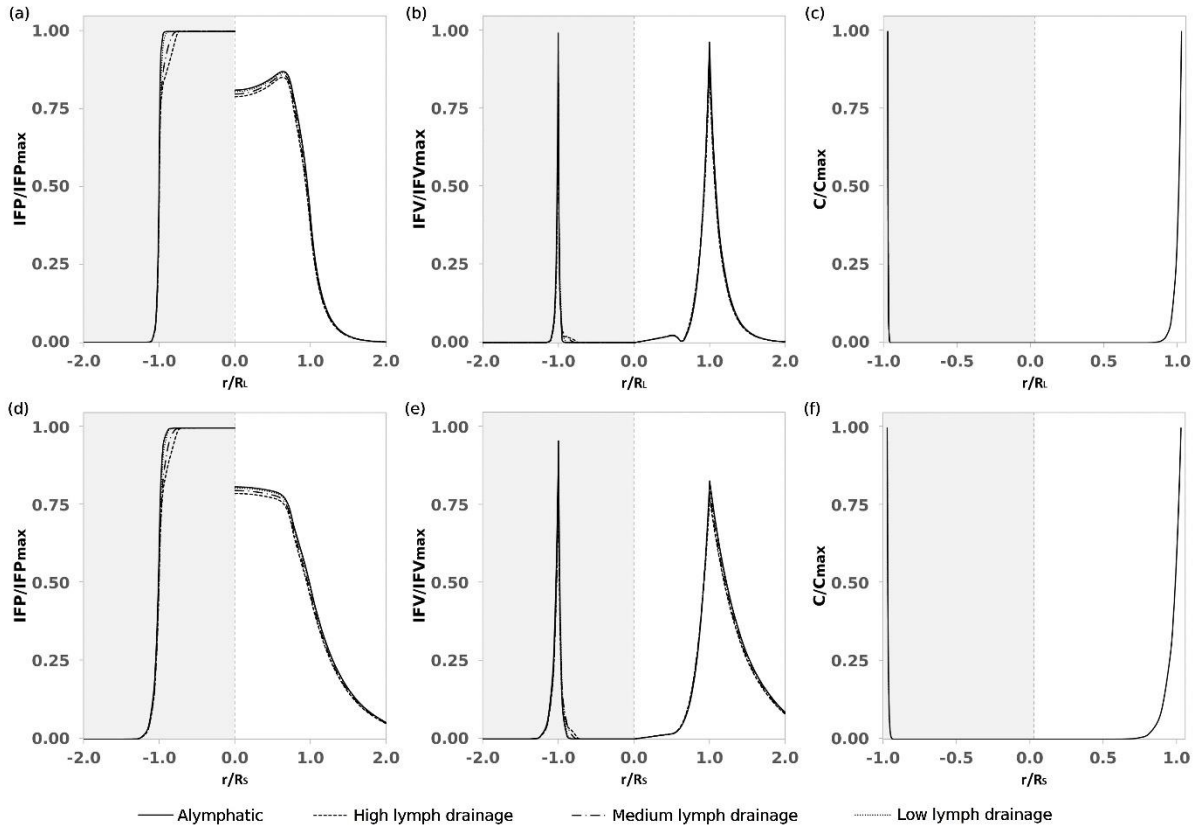

Fig S2. Effect of presence of lymphatic drainage on the (a, d) IFP, (b, e) IFV and (c, f) drug penetration in the SET category on (a-c) long and (d-f) short axes in a large tumor (D=50 mm; grey zone) and a small tumor (D=5 mm; white zone).

Fig. S2 demonstrates the role of lymphatic vessels in SETs. Similar trends were seen in both IFP and IFV profiles compared with the SSTs. The main difference in the IFP profile was that in the large tumor the plateau region was shorter in SETs comparing to SSTs (Fig. S2a,d). The IFV was also decreased with lymph vessels at the periphery (Fig. S2b,e). However, a similar form of the IFV profiles in both the small and the large tumors produces similar drug penetration profiles in all cases (Fig. S2c,f).

Fig. S3 demonstrates the lymphatic drainage effect on IFP, IFV and drug delivery to AETs. The implications on the IFP profile showed various trends between the large and the small tumor as well as on the long and short axes (Fig. S3a,d,g,j). Similar to symmetric tumors (SSTs and SETs), generally the IFP decreases with respect to lymphatic drainage functionality at the periphery region for the large tumor, and the central region for the small tumor. However, as illustrated in Fig. S3j, the IFP profile alteration in the small AET can get to the periphery region. The IFV profiles in AETs also demonstrated heterogeneous behaviors in each AET and on each axis, but generally showed the decreasing effect of lymphatic drainage on the IFV. However, same as symmetric tumors, no clear change was seen in the penetration profile regarding the presence of lymphatic vessels (Fig. S3c,f,i,l). this can be explained by the fact that the magnitude of opposing IFV profiles was comparable in all cases, resulting in the cancelation of the convective transport of the drug.

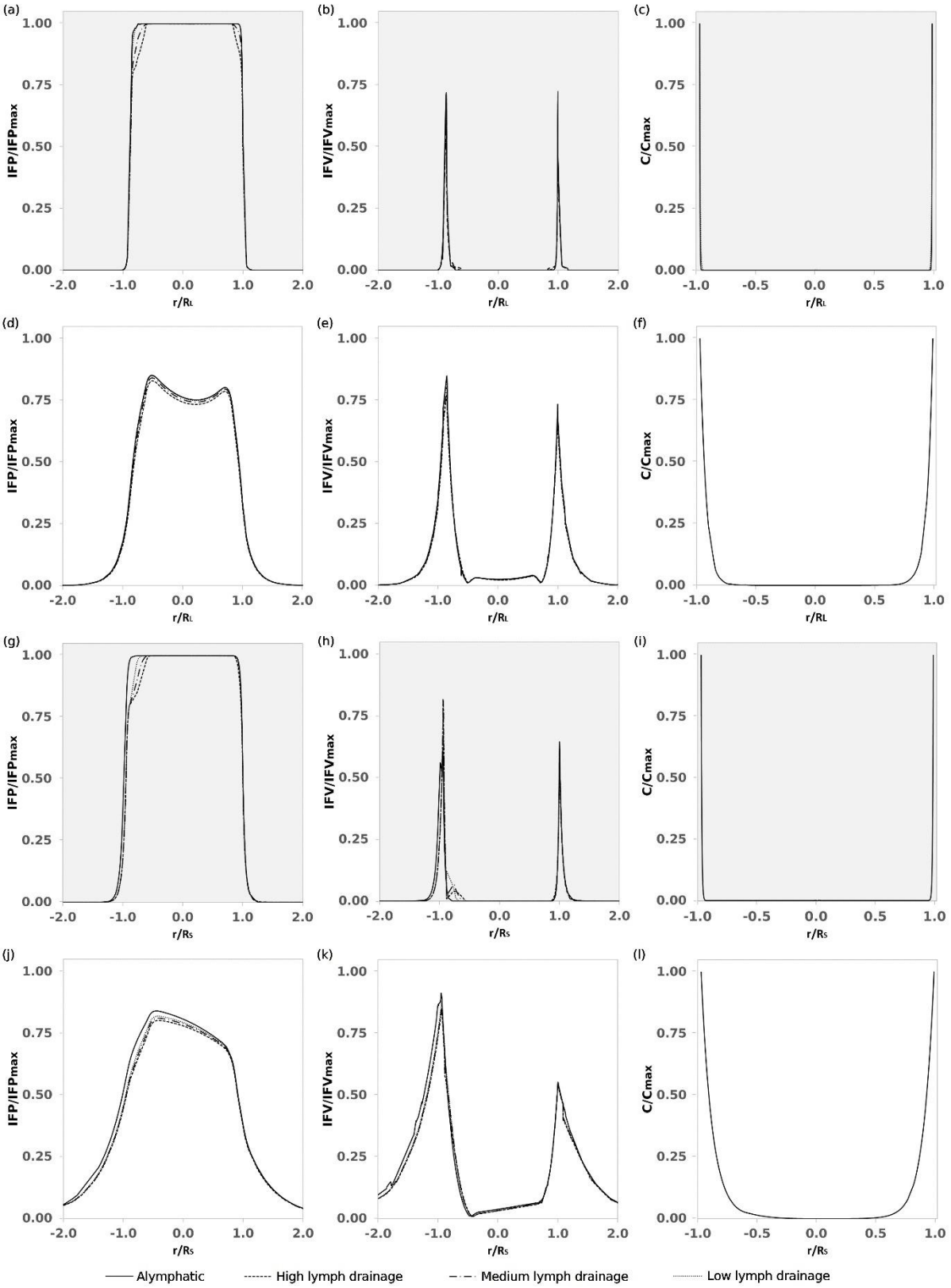

Fig S3. Effect of presence of lymphatic drainage on the (a, d, g, j) IFP, (b, e, h, k) IFV and (c, f, i, l) drug penetration in the AET category on (a-f) long and (g-l) short axes in a large tumor (D=50 mm; grey zone) and a small tumor (D=5 mm; white zone).